14 Weak Gravitational Lensing

David Wittman, Bhuvnesh Jain, Douglas Clowe, Ian P. Dell'Antonio, Rachel Mandelbaum, Morgan May, Masahiro Takada, Anthony Tyson, Sheng Wang, Andrew Zentner

Weak lensing (WL) is the most direct probe of the mass distribution in the Universe. It has been applied successfully on many different scales, from galaxy halos to large-scale structure. These measurements in turn allow us to constrain models of dark matter, dark energy, and cosmology. The primary limitation to date has been statistical: Lensing causes a small perturbation to the initially random orientations of background galaxies, so large numbers of background galaxies are required for high signal-to-noise ratio measurements. The LSST survey, encompassing billions of galaxies, will dramatically improve the statistical power of weak lensing observations. At large scales, cosmic variance is the limiting factor, and the extremely wide footprint of the LSST survey will bring this limit down as well. At the same time, the greatly increased statistical power means that systematic errors must be carefully examined and controlled.

The key observables to be extracted from the LSST data set are shear from galaxy shapes and source redshifts from photometric estimates. These must be derived for as many galaxies as possible, over as wide a range in redshift as possible. Subsequent analysis can be in terms of two- or three-point correlation functions, or shear profiles or mass maps depending on the specific project, but nearly all analyses rest on these two fundamental quantities. The projects are listed below in increasing order of angular scale. In combination (and especially when combined with LSST baryon acoustic oscillation data normalized by Planck data; § 15.1), these WL measurements will provide powerful constraints on dark energy and modified gravity, the mass power spectrum, and on the distribution and mass profiles of galaxy and cluster halos. Due to its precision and wide-area coverage, the LSST WL survey data will uniquely probe the physics of dark matter and cosmological issues of large-scale isotropy. Below, after reviewing weak lensing basics (§ 14.1), we discuss lensing by galaxies (§ 14.2), lensing by clusters of galaxies (§ 14.3), lensing by large scale structure (§ 14.4), and finally systematic issues which touch on all these areas (§ 14.5).

14.1 Weak Lensing Basics

Massive structures along the line of sight deflect photons originating from distant galaxies. Figure 12.1 shows the geometry in the general case where multiple photon paths from source to observer are possible. Outside the densest lines of sight, only one, slightly deflected, path is possible, and this is the domain of weak lensing. If the source is small compared to the scales on which the deflection angle varies, the effect is a (re)mapping of $f^{\rm s}$, the source's surface brightness distribution (see Bartelmann & Schneider 2001 for more details):

$$f^{\rm obs}(\theta_i) = f^{\rm s}(\mathcal{A}_{ij}\theta_j), \tag{14.1}$$

where $\mathcal{A}$ is the distortion matrix (the Jacobian of the transformation)

$$\mathcal{A} = \frac{\partial(\delta\theta_i)}{\partial\theta_j} = (\delta_{ij} - \Psi_{,ij}) = \begin{pmatrix} 1-\kappa-\gamma_1 & -\gamma_2 \\ -\gamma_2 & 1-\kappa+\gamma_1 \end{pmatrix}. \tag{14.2}$$

Here Ψ is the two-dimensional lensing potential introduced in Equation 12.5, and $\Psi_{,ij} \equiv \partial^2\Psi/\partial\theta_i\partial\theta_j$. The lensing convergence κ, defined in Equation 12.7, is a scalar quantity which can also be defined as a weighted projection of the mass density fluctuation field:

$$\kappa(\boldsymbol{\theta}) = \frac{1}{2}\nabla^2\Psi(\boldsymbol{\theta}) = \int d\chi W(\chi)\delta[\chi, \chi\boldsymbol{\theta}], \tag{14.3}$$

where the Laplacian operator $\nabla^2 \equiv \partial^2/\partial\boldsymbol{\theta}^2$ is defined using the flat sky approximation, δ is the fractional deviation of the density field from uniformity, and χ is the co-moving distance (we have assumed a spatially flat Universe). Note that χ is related to redshift z via the relation $d\chi = dz/H(z)$, where $H(z)$ is the Hubble parameter at epoch z. The lensing efficiency function W is given by

$$W(\chi) = \frac{3}{2}\Omega_{m0}H_0^2 a^{-1}(\chi)\chi \int d\chi_s\, n_s(\chi_s)\frac{\chi_{\rm s}-\chi}{\chi_s}, \tag{14.4}$$

where $n_s(\chi_s)$ is the redshift selection function of source galaxies and H_0 is the Hubble constant today. If all source galaxies are at a single redshift z_s, then $n_s(\chi) = \delta_D(\chi - \chi_s)$.

In Equation 14.2 we introduced the components of the complex shear $\boldsymbol{\gamma} \equiv \gamma_1 + i\gamma_2$, which can also be written as $\boldsymbol{\gamma} = \gamma\,\exp(2i\alpha)$, where α is the orientation angle of the shear. The Cartesian components of the shear field are related to the lensing potential through

$$\gamma_1 = \frac{1}{2}(\Psi_{,11} - \Psi_{,22}) \quad \text{and} \quad \gamma_2 = \Psi_{,12}. \tag{14.5}$$

In the weak lensing regime, the convergence κ gives the magnification (increase in size) of an image and the shear γ gives the ellipticity induced on an initially circular image (see Figure 14.1 for an illustration). Under the assumption that galaxies are randomly oriented in the absence of lensing, the strength of the tidal gravitational field can be inferred from the measured ellipticities of an ensemble of sources (see § 14.5.3 for a discussion of intrinsic alignments). In the absence of observational distortions, the observed ellipticity, $e^{\rm obs}$, is related to its unlensed value, $e^{\rm int}$, through (Seitz & Schneider 1997; Bartelmann & Schneider 2001):

$$e^{\rm obs} = \frac{e^{\rm int} + \gamma}{1 + \gamma^* e^{\rm int}}, \tag{14.6}$$

where $e \simeq [(1-b/a)/(1+b/a)]\exp(2i\alpha)$ for an ellipse with major and minor axes, a and b, respectively and orientation angle α. γ^* is the complex conjugate of the lensing shear. The average value of $e^{\rm obs} \approx \gamma$ in the weak lensing regime. To be more precise, the observable is the reduced shear $\gamma/(1-\kappa)$. Hence, the unbiased measurement of the shapes of background galaxies (which

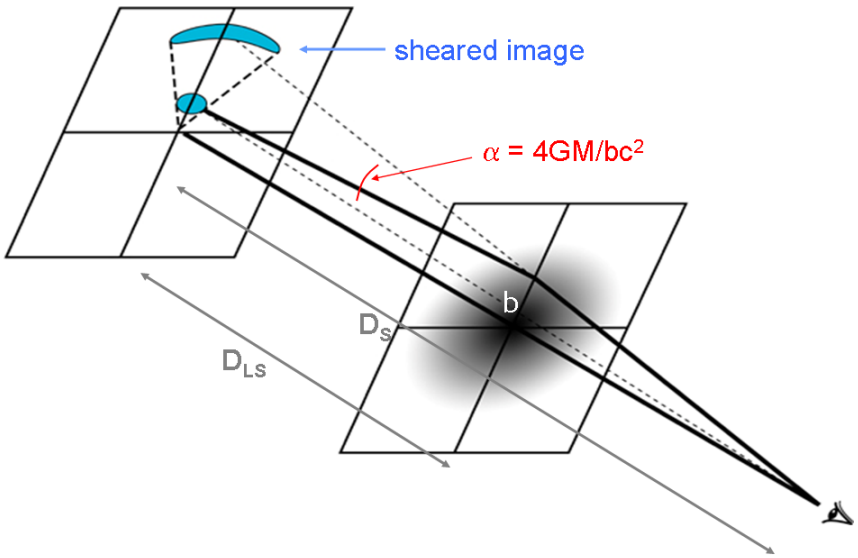

Figure 14.1: The primary observable effect of weak lensing is to impose an apparent tangential ellipticity on background galaxies which are truly randomly aligned.

constitute the small, faint end of the galaxy sample) lies at the heart of any weak lensing analysis. Some of the difficulties inherent in this task are discussed in § 14.5.

Shear and magnification are both observable. Shear is inferred from the distribution of galaxy *shapes*; it is assumed that galaxy shapes are randomly distributed in the absence of lensing (but see § 14.5.3 for violations of that assumption and how they may be dealt with). More concretely, if galaxies are approximated as ellipses with ellipticity, ϵ_i, and position angles, ϕ_i, then the ellipticity components, $\epsilon_{1,i} \equiv \epsilon_i \cos(2\phi_i)$, and $\epsilon_{2,i} \equiv \epsilon_i \sin(2\phi_i)$ are randomly distributed with zero mean. Shifts away from zero mean are proportional to the shear (about a 1% effect in a typical area of sky), but the constant of proportionality depends on various factors, thus making *shear calibration* a potential source of systematic error (discussed in § 14.5.2). In addition, the intrinsic spread presents a source of noise, *shape noise*, which can only be reduced by averaging together more galaxies per unit area of sky. We can write the shear noise in a one-arcminute patch of sky as $\gamma_{\rm rms}/\sqrt{N_{\rm eff}}$, where $\gamma_{\rm rms}$ encodes the shape noise, which we take to be $0.4/\sqrt{2} = 0.28$ per component, and $N_{\rm eff}$ is the effective number of galaxies. The effective number of galaxies is defined to account for the fact that many galaxies are imaged at low S/N and therefore do not fully contribute to beating down the shape noise. The effective number is the number of perfectly measured galaxies which would be required to yield the same shear noise as the actual set of measured galaxies:

$$N_{\rm eff} = \sum_{i=1}^{n_{gals}} \frac{\sigma_{SN}^2}{\sigma_{SN}^2 + \sigma_{meas,i}^2}, \tag{14.7}$$

are themselves imperfectly measured where $\sigma_{meas,i}$ is the measurement error on the shape of the ith galaxy and σ_{SN} is the rms shape noise (distinct from $\gamma_{\rm rms}$ only because this calculation is in shape rather than shear space).

Contributions to $\sigma_{meas,i}$ come from photon noise and from finite angular resolution. Photon noise determines the uncertainty in measuring the shape as observed after convolution with the PSF. This uncertainty is then amplified when extrapolating to the true pre-PSF shape, by a factor which depends on the relative sizes of the galaxy and the PSF, but which is never less than unity. Therefore, to maximize the effective number of galaxies, a survey must go deep and have good angular resolution. LSST will have both, and will maximize angular resolution by taking data in r and i (the most sensitive bands and the ones to be used for lensing) only when the seeing is better than $0.7''$.

How many galaxies per square arcminute will LSST effectively measure, and what shear noise level will it reach? Figure A.1 of Clowe et al. (2006b) shows the shear noise level in 45-minute and 2-hour exposures taken with the 8.2-m VLT in various seeing conditions. These data show that for LSST resolution and depth in r *or* i band (slightly better than $0.7''$, maintained over 200 30-second visits) the shear noise is 0.05 arcmin^{-2}; this corresponds to $N_{\rm eff} = 31$ galaxies arcmin^{-2} for our fiducial $\gamma_{\rm rms}$. $N_{\rm eff}$ will be increased by combining information from multiple filters, boosting more galaxies above the useful S/N threshold. Jarvis & Jain (2008) showed that the number density scales as the square root of the number of filters, assuming the filters are roughly equally deep. Counting only r and i for LSST, this yields $N_{\rm eff} = 44\,{\rm arcmin}^{-2}$. The actual gain is likely to be somewhat lower because the additional galaxies will be the least well resolved and the most affected by crowding, background estimation errors, etc, and so we adopt $N_{\rm eff} = 40\,{\rm arcmin}^{-2}$ in the sections below. We emphasize that LSST will detect many more galaxies, as estimated in § 3.7.2; this is the effective number usable for weak lensing.

We are now beginning to analyze high-fidelity simulations (§ 3.3), which will give us more concrete numbers for LSST data (including the redshift distribution, not just the overall number, of usable galaxies). The statistical errors over 20,000 deg^2, even including cosmic variance, are very small and naturally raise the question of the systematic error floor. This is a primary concern of the weak lensing collaboration, and we devote § 14.5 to it.

Measuring magnification is more difficult than shear because the unlensed distribution of galaxy fluxes is roughly a power law, making it difficult to measure the small departures induced by lensing. It has been observed and can be used in some cases to break degeneracies involved in using shear alone, but by and large weak lensing projects focus almost exclusively on shear. Magnification will find some uses in the cluster context, but as far as large-scale statistics are concerned, magnification can only be measured as a cross-correlation with foreground galaxies (and so far with lower signal-to-noise ratio than the shear). Whether this will prove to be a useful complementary measure of lensing for LSST remains to be determined.

14.2 Galaxy-Galaxy Lensing

Rachel Mandelbaum

14.2.1 Motivation and Basic Concepts

Weak lensing around galaxies (or galaxy-galaxy lensing, hereafter, g-g lensing) provides a *direct* probe of the dark matter that surrounds galaxies (for a review, see Bartelmann et al. (2001); see also § 9.5 for a galaxy-based view of some of the issues examined here). Gravitational lensing induces tangential shear distortions of background galaxies around foreground galaxies, allowing direct measurement of the galaxy-mass correlation function around galaxies. The distortions induced by individual galaxies are small (on the order of 0.1%), but by averaging over all foreground galaxies within a given subsample, we obtain high signal-to-noise ratio in the shear as a function of angular separation from the galaxy. If we know the lens redshifts or some approximation thereof (e.g., photometric redshift estimates), the shear signal can be related to the projected mass density as a function of proper distance from the galaxy. Thus we can observe the averaged dark matter distribution around any given galaxy sample.

Mathematically, g-g lensing probes the connection between galaxies and matter via their cross-correlation function

$$\xi_{gm}(\vec{r}) = \langle \delta_g(\vec{x}) \delta_m(\vec{x}+\vec{r}) \rangle, \tag{14.8}$$

where δ_g and δ_m are overdensities of galaxies and matter respectively. This cross-correlation can be related to the projected surface density,

$$\Sigma(R) = \overline{\rho} \int \left[1 + \xi_{gm}\left(\sqrt{R^2+\chi^2}\right)\right] d\chi \tag{14.9}$$

(for $r^2 = R^2 + \chi^2$), where we ignore the radial window, which is much broader than the typical extent of the lens. This surface density is then related to the observable quantity for lensing,

$$\Delta\Sigma(R) = \gamma_t(R)\Sigma_c = \overline{\Sigma}(< R) - \Sigma(R), \tag{14.10}$$

where the second relation is true only for a matter distribution that is axisymmetric along the line of sight. This observable quantity can be expressed as the product of two factors, a tangential shear, γ_t, and a geometric factor, the critical surface density

$$\Sigma_c = \frac{c^2}{4\pi G} \frac{D_S}{D_L D_{LS}}, \tag{14.11}$$

where D_L and D_S are angular diameter distances to the lens and source, D_{LS} is the angular diameter distance between the lens and source. Note that the κ defined in § 14.1 is equal to $\frac{\Sigma}{\Sigma_c}$.

Typical practice is to measure the g-g weak lensing signal around a stacked sample of lenses to obtain the average $\Delta\Sigma(R)$ for the whole sample, as the signal from a individual galaxy is too weak to be detected over the shape noise. For shallow surveys it may be necessary to stack tens of thousands of galaxy-mass lenses to obtain reasonable S/N (Mandelbaum et al. 2006c); clearly, for the much deeper LSST, an equal S/N can be achieved by stacking far fewer lenses, thus allowing finer divisions in galaxy properties and more information to be extracted. This stacked lensing signal can be understood in terms of what information is available on different scales. The lensing signal on $\lesssim 0.3h^{-1}$Mpc scales tells us about the dark matter halo in which the galaxy resides; the signal from $\sim 0.3 - 1h^{-1}$Mpc reveals the local environment (e.g., group/cluster membership) of the galaxy; and the signal on larger scales indicates the large-scale correlations of the galaxy sample, similar to the information present in the galaxy-galaxy autocorrelations.

The shear systematics requirements for g-g lensing are less rigorous than for cosmic shear because g-g lensing is a cross-correlation function. As a result, if the shape measurements of galaxies used to compute the shear have some multiplicative and additive bias, the additive bias term can be entirely removed through cross-correlation with a random lens sample, and the multiplicative bias enters only once.

14.2.2 Applications with LSST

Galaxy-galaxy lensing on its own can be used to explore many properties of galaxies, to relate them to the underlying host dark matter halos and, therefore, to constrain galaxy formation and evolution. Below are two examples of applications of g-g lensing.

Galaxy Host Halo Mass as a Function of Stellar Mass

After estimating the stellar mass of galaxies (using luminosities and colors) and binning the galaxies by stellar mass, it is possible to study the lensing properties of the galaxies as a function of stellar mass. The results would provide important information about the connection between the visible (stellar) component of the galaxy, and its underlying dark matter halo. Thus, they would be very useful for constraining theories of galaxy formation and evolution.

This procedure has been done in several surveys at lower redshift, such as SDSS (see Figure 14.2, Mandelbaum et al. 2006c) and RCS (Hoekstra et al. 2005), and as high as $z = 0.8$ but with relatively low S/N using GEMS (Heymans et al. 2006a). LSST will have the power to vastly improve the precision of these constraints, which would be particularly interesting at the low stellar mass end, below $L \sim L_*$, where these previous surveys lack the statistical power to make any interesting weak lensing constraints (and where strong lensing constraints are unlikely because lower mass galaxies are typically not strong lenses). Furthermore, LSST will enable studies to at least a lens redshift $z \sim 1$, thus giving a measure of galaxy mass assembly and the relation between stellar and halo mass over the second half of the lifetime of the universe. Finally, LSST will be able to extend all these measurements out to much larger angular scales, up to $10h^{-1}$ Mpc, with high S/N.

Halo Ellipticity

Dark matter halo ellipticity, a robust prediction of ΛCDM according to N-body and hydrodynamic simulations, can in principle be detected using galaxy-galaxy weak lensing. Ellipticity of dark matter halo profiles has been predicted in CDM N-body simulations (e.g., Dubinski & Carlberg 1991), and observed with non-lensing methods on scales < 20 kpc (for a review, see Sackett 1999).

Given the need to stack multiple objects, a measurement of dark matter halo ellipticity naturally depends on alignment between the ellipticity of the light distribution and of the matter distribution. Current measurements have relatively poor signal-to-noise ratio (Hoekstra et al. 2004; Mandelbaum et al. 2006a; Parker et al. 2007) though there is a suggestion of halo ellipticity in CFHTLS data and for very luminous red galaxies in SDSS. A robust measurement of halo ellipticity would both confirm the predictions of simulations, and serve as a measurement of the alignment between the light and mass distributions in galaxies, which is in itself an important clue to environmental

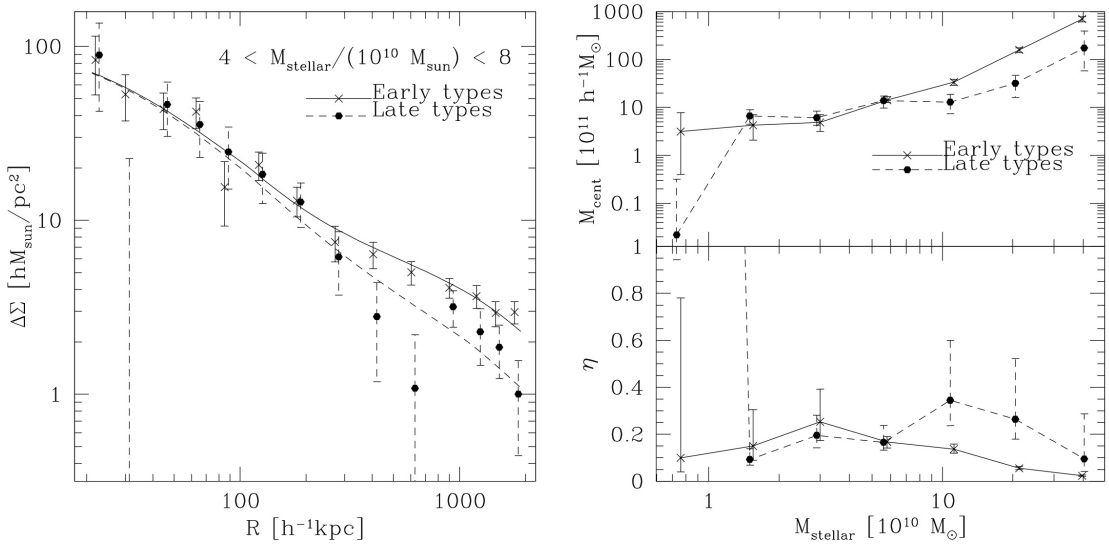

Figure 14.2: At left, measured lensing signal from SDSS for a stellar mass bin containing Milky Way-type galaxies, with a model shown as the smooth lines. Such fits were used as input for the figure at the right, which shows central halo mass (top) and conversion efficiency in central galaxy $\eta = (M_*/M_{halo})/(\Omega_b/\Omega_m)$ (bottom) as a function of stellar mass for early-type and late-type galaxies. Constraints are extremely weak for galaxies with low stellar mass and for the relatively rare high stellar mass late-type galaxies. Figure uses data originally published in Mandelbaum et al. (2006c).

effects on galaxy shapes during their formation and evolution. Again, due to the depth of LSST, it should be possible to explore the ellipticity of dark matter halos as a function of galaxy type and of redshift to unprecedented precision relative to what is possible now. These results may also be a stringent test of the theory of gravity particularly for isolated halos (Milgrom 1983; Sanders 1986).

14.2.3 Combining Galaxy-Galaxy Lensing with Galaxy Clustering

Galaxy-galaxy lensing is a powerful probe of cosmological parameters when combined with measurements of the clustering of galaxies. The former measures the galaxy-mass correlations, ξ_{gm}, whereas the latter measures the galaxy autocorrelations, ξ_{gg}. On large scales, where the mass and galaxy fluctuations are highly correlated (though with possible multiplicative offsets in amplitude, known as "galaxy bias"), the two probes together can be used to estimate the matter correlation function, ξ_{mm}. Furthermore, the galaxy bias estimated in this way is not limited by cosmic variance, because the same exact density fluctuations are used for both measurements. Because the systematics in g-g lensing are different than in cosmic shear, this measurement is a useful cross-check on the matter power spectrum reconstructed from cosmic shear.

14.3 Galaxy Clusters

Clusters of galaxies are the largest virialized structures in the Universe and are useful both as cosmological probes and as astrophysical laboratories in their own right. The two aspects are heavily intertwined, because we must understand the physical processes in clusters to have confidence that they can be used as accurate cosmological probes. Readers interested in the astrophysical laboratory aspect are referred to § 13.6 and § 9.5 respectively.

Clusters represent the most extreme overdensities, and thus probe the growth of structure. An accurate census of clusters by mass and redshift can thus be used to infer cosmological parameters. Weak lensing can play a critical role here because it can measure total cluster mass without regard to baryon content, star formation history, or dynamical state. Thus, even if clusters are discovered by optical, X-ray, or Sunyaev-Zel'dovich (SZ) surveys, lensing is crucial for calibrating the mass-observable relation. § 13.6 explores in more detail searches for clusters in the galaxy distribution and the synergies with future surveys at other wavelengths. Weak lensing studies of clusters also naturally complement the studies of cluster-scale strong lensing (§ 12.12). Strong lensing reconstructions of mass distributions in the cluster cores can eliminate mass sheet degeneracies in the weak lensing measurements (Broadhurst et al. 1995), allowing more accurate total masses to be calculated. At the same time, weak lensing measurements are essential to refining models for the mass distribution and substructure in cluster cores (Bradač et al. 2006).

We focus here on what weak lensing measurements of clusters of galaxies with LSST will mean for the study of the properties of clusters themselves. First, we examine mass measurements of individual clusters. Then, we briefly discuss *searching* for clusters with lensing, and finally we generalize this to a search for peaks in the shear field, regardless of whether they are truly clusters of galaxies. We show that the shear peak distribution revealed by LSST will provide a powerful probe of cosmology.

14.3.1 Cluster Mass Distributions

Douglas Clowe, Ian P. Dell'Antonio

LSST will generate the largest and most uniform sample to date of galaxy clusters with gravitational lensing measurements. This sample of clusters will be important for cosmological measurements and for the study of the assembly history of galaxy clusters.

At their most basic level, the cluster weak lensing measurements will consist of measurements of shapes, magnitudes, and colors (and hence photometric redshift estimates) for ~ 40 galaxies arcmin^{-2} behind the clusters (for low redshift clusters at least; some of these galaxies will be in front of higher redshift clusters, and so would not be distorted). These measurements can be combined many different ways to constrain the mass profiles of clusters and the mass distribution in clusters. For the regions of sky that comprise the LSST deep fields (§ 2.1), we expect almost 70% more resolved galaxies, with much more precise SED measurements for them. These deep fields will be very useful as calibrators of the contamination at the faint end of the LSST weak lensing mass distribution.

14.3.2 One-dimensional Cluster Lensing: Radial Cluster Profile Fitting

The mean radial density profile of clusters can be calculated from the azimuthally averaged tangential reduced shears of the background galaxies (e.g., Tyson et al. 1990). The deflection of a galaxy at an observed radius, r, from the cluster center is a function of the enclosed mass. Because the distortion of a galaxy is a function of the deflection and its gradient, the tangential shear as a function of radius encodes information about the slope of the profile.

In these one-dimensional measurements (and also in two-dimensional lensing maps), the quantity that is calculated depends on the line-of-sight surface density (the integral of the mass density along the line of sight) modulated by the changes in $\Sigma_{\rm crit}$ with the redshift of the mass. As a result, all of these techniques are sensitive to projection effects whereby unrelated (and often quite distant) structures along the line-of-sight contribute to the signal. Some progress can be made in disentangling the signal along the line of sight using photometric redshifts, but in general there is always contamination because the redshift dependence of the lensing kernel is weak, and because large-scale structure at very similar redshift to the target clusters cannot be resolved by photometric redshifts. Nevertheless, one-dimensional techniques can provide powerful (and comparatively high S/N) measures of cluster properties.

Two complementary approaches have been introduced to recover the mass distribution from the shear profile. Fahlman et al. (1994) introduced a non-parametric technique of "aperture densitometry," based on the realization that the difference between the mean surface mass density inside a radius, R, and the mean surface mass density out to some fiducial outer annulus or radius, R_m, is given by an integral over the (seeing-corrected) tangential shear between R and R_m:

$$\zeta = \bar{\kappa}(r < R) - \bar{\kappa}(R < r < R_m) = \frac{2}{(1 - R^2/R_m^2)} \int_R^{R_m} \langle \gamma_T \rangle d\ln r. \tag{14.12}$$

The $\langle\rangle$ notation indicates an azimuthally averaged value around a chosen cluster center. A variant on this statistic which uses a fixed outer aperture instead of one which extends all the way to R is:

$$\zeta_c = \bar{\kappa}(r < R_1) - \bar{\kappa}(R_2 < r < R_m) = 2 \int_{R_1}^{R_2} \langle \gamma_T \rangle d\ln r + \frac{2}{(1 - R_2^2/R_m^2)} \int_{R_1}^{R_m} \langle \gamma_T \rangle d\ln r, \tag{14.13}$$

where R_1 is the radius inside which one is measuring the mean surface density and R_2 is the radius of the inner edge of the fixed outer aperture (Clowe et al. 2000). In the case where $R_m \gg R_1, R_2$, as can be the case for LSST studies, these two statistics become identical and the error on both is simply $\sigma_\zeta = \sigma_\gamma / \sqrt{\pi R_1^2 n}$, where n is the number density of background galaxies in the survey. From this we get an estimate for LSST that $\sigma_\zeta = 0.028/R_1$ with R_1 measured in arcseconds. As with κ, one can convert this to a surface density by multiplying by $\Sigma_{\rm crit}$.

The aperture densitometry technique has the advantage of being non-parametric. However, it is limited by the extent to which the outer annulus can be measured (which has been a limiting factor up to now but will be a non-issue given LSST's sky coverage). Furthermore, a radial profile made from ζ has points that are strongly correlated, and it provides only a measurement of the integrated surface density with no way to convert to a three-dimensional mass density profile. Finally, the above analysis assumes that one is measuring the shear γ when in fact one measures the reduced shear $g = \gamma/(1 - \kappa)$. This latter effect leads to severe overestimation of the surface density of clusters in their cores.

A related statistic which can be used to compute κ as a function of radius is:

$$\kappa(R) = 1 - \frac{1}{1 - g(R)} \exp\left(- \int_R^{R_m} \frac{2\langle g \rangle}{r(1 - \langle g \rangle)} dr - \frac{2\langle g(R_m) \rangle}{\alpha} \right), \tag{14.14}$$

which assumes that at $r > R_m$ the reduced shear profile behaves as a power law, $\langle g(r) \rangle \propto r^{-\alpha}$ (Clowe & Schneider 2001). This assumption is usually the limiting factor in the accuracy of this statistic outside of the cluster core. For the LSST survey, however, R_m can be made so large that $\langle g(R_m) \rangle \to 0$ and, therefore, the effect of the power-law assumption is negligible. While this statistic properly uses g instead of γ and is, therefore, valid in massive cluster cores, it is still a measurement of the surface density, the individual radial κ points are still strongly correlated, and one is still sensitive to superposition of unrelated structures along the line-of-sight. A final statistic in this family is the aperture mass statistic (Schneider et al. 1998), which sums up $\langle g \rangle$ convolved with a given radial kernel over a given aperture, and is mostly used to detect mass peaks and measure their significance of detection in a non-parametric method.

Alternatively, one can use parametric fitting techniques in which a parametrized radial profile family (usually as an NFW profile) is assumed, and the measured tangential reduced shear is compared to the model to fit the parameters of the model (e.g., Clowe & Schneider 2001). Although the choice of model family can affect the results (because the model is "forced" to follow the profile even in the presence of other signals such as extra substructure), this technique allows one to convert the two-dimensional lensing measurement to a three-dimensional density measurement assuming the chosen model family is valid. It also allows for an easier calculation of the significance of measurement, as one can easily compute a $\Delta\chi^2$ between the best fit model and a zero mass model or similar statistic. The primary uncertainties with this technique, aside from the noise in the shear measurement and the question about whether the assumed mass profile family is valid, are the triaxiality in the cluster population (the model families are usually spherically symmetric) and the presence of significant mass substructure. Despite the biases, one-dimensional measurements will provide the highest significance detections of the lowest mass systems. With LSST, we should be able to measure the masses of clusters with mass $M_{200} > 1.5 \times 10^{14}\, M_\odot$ to 10% statistical accuracy. Given the area coverage of LSST, this level of accuracy will be reached for approximately 20,000 clusters of galaxies (Hamana et al. 2004). To measure the mean properties of even less massive systems, we can combine the tangential shear around large samples of systems selected through optical, X-ray, or SZ techniques. This "stacking" (Sheldon et al. 2001, 2007; Johnston et al. 2007) of clusters sorted according to an observable will allow the precise calibration of the relationship between mass and observable (§ 12.12).

Systematic errors arise in individual clusters due to projection effects, both non-local (multiple clusters or groups widely separated along the line-of-sight) and local (clusters embedded in local large-scale structure). The availability of accurate photometric redshift information will allow the calibration of the first of the two projection effects, but the second effect will remain an irreducible source of error in the mass measurements. Other sources of error include intrinsic alignments (Mackey et al. 2002; see § 14.5.3), although these can be minimized with the photometric redshift information (Heymans et al. 2004) and effects from the triaxiality and substructure within individual clusters. Because a one-dimensional treatment necessarily averages over the actual distribution of matter, it will produce a biased measurement for systems that depart greatly from

spherical symmetry. While the stacking or shear cross-correlation methods mentioned above can remove these effects for mean measurements of large samples, they are not applicable to the study of individual systems, which will be subject to bias due to departures from spherical symmetry. To deal with this bias, two-dimensional weak lensing techniques will need to be employed. Nevertheless, because one-dimensional lensing can be used to detect lower mass systems, one-dimensional measures will be essential for constructing the cluster mass function both in a fixed redshift range and as a function of redshift (which provides an independent test of hierarchical clustering).

14.3.3 Two-dimensional Cluster Lensing Maps

Given a catalog of galaxy positions, sizes and reduced shears, one can construct a two-dimensional map of the convergence either directly through a convolution of the reduced shears with a window function (Kaiser & Squires 1993; Kaiser et al. 1995; Tyson & Fischer 1995) or indirectly by modeling the gravitational potential and matching the predicted shear to the observations (Seitz & Schneider 1996; Seitz et al. 1998; Bradač et al. 2005; Khiabanian & Dell'Antonio 2008). The resulting map can be used to detect samples of clusters and the cluster mass function for cosmological purposes (§ 12.12), but also to study the distribution of mass in individual clusters. In particular, LSST will be sensitive (at roughly 4σ) to individual clusters with $\sigma > 500$ km s^{-1} or $M_{200} > 0.5 \times 10^{14} M_{\odot}$. Furthermore, the weak lensing data will lead to detection of substructures with M/M_{cl} greater than 10% for approximately 10^4 clusters of galaxies with $0.05 < z < 0.7$. This large sample will be an extremely important comparison set to match with the gravitational clustering simulations (Springel et al. 2005) to constrain the growth of structure, and to compare with the galaxy spatial and star formation distribution to study the evolution properties of galaxies as a function of *mass* environment. Just as fundamentally, the LSST measurements of these clusters will determine mass centroids for these clusters accurate to better than 1 arcminute. These centroids can be compared with the optical and x-ray centroids of the cluster to determine whether there are offsets between the various components. The presence of mass offsets in merging clusters provides a sensitive test of modified gravity theories (Clowe et al. 2006a; see also § 12.7).

14.3.4 Magnification by Clusters

LSST will also study the magnification induced by cluster lenses. Unlike shear, magnification is not affected by the mass-sheet degeneracy (§ 12.1). This means that magnification measurements can be combined with shear measurements to calibrate the masses of clusters derived from shear lensing, even in the absence of any strong lensing features. Although there have been attempts to use magnification to determine the properties of clusters (cf. Broadhurst et al. 1995), it is difficult to measure for two reasons. First, the competing effects of the dilution of objects due to the magnification of the background area and the increase in detected objects due to the magnification means that for different classes of objects, the magnification can either enhance or decrease the number counts at a given flux level. More seriously unlike shear lensing, there is not an a priori determination of what the unmagnified population should look like. However, LSST will probe a significant fraction of the observable Universe at these redshifts, allowing the mean number density of galaxies to be measured to great accuracy. Stacking a large number of clusters, LSST will be able to measure the mean magnification for the ensemble of clusters $M_{vir} > 5 \times 10^{14}\ M_{\odot}$ and

$0.1 < z < 0.6$ (of which LSST should detect ~ 3000) with a statistical error smaller than 0.2% (of course, the systematic errors in field-to-field photometric calibration will likely limit the overall mass scale calibration to $\sim 1\%$.)

One of the systematic sources of uncertainty in magnification measurements is ignorance about the number counts of objects in the magnitude range immediately below the magnitude limit of the survey. Here, the LSST deep fields will prove exceptionally valuable – they will cover enough area to reach a representative sample of the faint Universe, and will allow accurate estimates of the population of galaxies up to 1 magnitude deeper than the main survey. This should reduce the contribution of the unknown slope of the number counts to the magnification calculation below the 1% level.

14.3.5 Three-dimensional Cluster Lensing

We can study the variation of the shear signal from clusters as a function of photometric redshift (§ 3.8), which allows fundamentally new science. First, it provides an independent technique for measuring the angular diameter distance to clusters. Wittman et al. (2003) have demonstrated that one can estimate the redshift of a galaxy cluster to an accuracy of roughly 0.1 simply based on the variation of the shear of the background galaxies with redshift. Second, the exact shape of the shear versus redshift profile is a function of the cosmological parameters. This has important consequences for cosmology. Jain & Taylor (2003) showed that for a large enough sample of clusters, one could use the variation of shear with redshift as a tomographic measurement. For a given foreground mass distribution, the measured shear at a fixed angular position (θ, ϕ) is only a function of the angular diameter distance ratio, $D_L D_{LS}/D_S$. Thus, the shear tomography provides a geometry-only measurement of the dark energy equation of state; a measurement that is complementary to the cosmological measurement derived from shear correlation functions.

Tomographic measurements such as these can also be used to test photometric redshift estimates for large samples of galaxies that are too faint to be measured spectroscopically. Using the ensemble of weak lensing detected clusters of galaxies, comparison of the shear vs. photometric redshift for galaxies both bright enough for spectroscopic confirmation and too faint for spectroscopy should allow the tomographic profile of the former to calibrate the redshift normalization for the latter, effectively extending the magnitude limit for verifying photometric redshift estimates by at least one magnitude.

14.3.6 Panoramic Mass Maps

The techniques for surface mass density reconstruction we've discussed will be applied to the entire 20,000 deg^2 LSST survey area, yielding a 2.5-dimensional atlas of "where mass is" that will simultaneously be useful to professional astronomers and fascinating for the public. Astronomers will use these maps to examine galaxy properties as a function of environment. "Environment" in this context is usually defined in terms of neighboring galaxies, but mass maps covering half the sky will enable a new way of looking at the concept of environment. With the LSST sample it will be possible to map galaxy bias (§ 14.2.3) over the sky, cross-correlate with the CMB to map

CMB lensing, and cross-correlate with supernovae to map (and possibly reduce the scatter due to) supernova lensing (§ 11.10).

Mass distributions are also important for testing alternative theories of gravity (§ 15.3). Unambiguous examples of discrepancies on large scales between the mass and galaxy distribution will not only constrain these theories, but will also derive astrophysical constraints on dark matter interaction cross sections, as was done for the visually stunning example of the Bullet Cluster (Markevitch et al. 2004, § 12.10).

At the same time, these maps are a prime opportunity to bring science to the public. Everyone understands maps, and the public will be able to explore mass (and other) maps over half the sky. The maps will also have some coarse redshift resolution, enabling them to gain a sense of cosmic time and cosmic history.

14.3.7 Shear-selected Clusters

The mass maps lead naturally to the idea of searching for clusters with weak lensing. Weak lensing has traditionally been used to provide mass measurements of already known clusters, but fields of view are now large enough(2–20 deg^2) to allow blind surveys for mass overdensities (Wittman et al. 2006; Dietrich et al. 2007; Gavazzi & Soucail 2007; Miyazaki et al. 2007; Massey et al. 2007b). Based on these surveys, a conservative estimate is that LSST will reveal two shear-selected clusters deg^{-2} with good signal-to-noise ratio, or 40,000 over the full survey area. Results to date suggest that many of these will not be strong X-ray sources, and many strong X-ray sources will not be selected by shear. This is an exciting opportunity to select a large sample of clusters based on mass only, rather than emitted light, but this field is currently in its infancy. Understanding selection effects is critical for using cluster counts as a cosmological tool (see Figure 12.22 and § 13.6) because mass, not light, clustering is the predictable quantity in cosmological models; simulations of structure formation in these models (§ 15.5) will be necessary to interpret the data. Shear selection provides a unique view of these selection effects, and LSST will greatly expand this view.

Because shear selection uses background galaxies rather than cluster members, it is difficult to detect clusters beyond $z \sim 0.7$. Hence the proposed deep LSST fields will be very useful in accumulating a higher redshift, shear-selected sample in a smaller (but still ~ 100 deg^2!) area. This will be critical in comparing with X-ray, optically, and SZ selected samples, which all go to higher redshift.

Shear selection has the property that it selects on *projected* mass density. Therefore, shear peaks may not be true three-dimensional density peaks. From a cluster expert's point of view, this results in "false positives," which must be eliminated to get a true shear-selected cluster sample. Using source redshift information to constrain the structure along the line of sight (tomography) helps somewhat but does not eliminate these "false positives" (Hennawi & Spergel 2005), because the lensing kernel is quite broad. We will see in the next section how to turn this around and use shear peaks as a function of *source* redshift (rather than lens redshift) to constrain cosmological parameters.

14.3.8 Cosmology with Shear Peaks

Sheng Wang, Morgan May

Structure formation is a hierarchical process in which gravity is constantly drawing matter together to form increasingly larger structures. Clusters of galaxies currently sit atop this hierarchy as the most massive objects that have had time to collapse under the influence of their own gravity. Their appearance on the cosmic scene is relatively recent, but they also serve as markers for those locations of the highest density fluctuations in the early Universe (Bardeen et al. 1986), which make them unique tracers of cosmic evolution (Haiman et al. 2001). Analytic predictions exist for the mass function of these rare events per unit co-moving volume per unit cluster mass (Press & Schechter 1974; Bond et al. 1991, see also Figure 12.22 and § 13.6). Gravitational N-body simulations can produce even more precise predictions of the mass function (Sheth & Tormen 1999; Jenkins et al. 2001, see also § 15.5).

The abundance of clusters on the sky is sensitive to dark energy in two ways: first, the co-moving volume element depends on dark energy, so cluster counts depend upon the cosmological expansion history; second, the mass function itself is sensitive to the amplitude of density fluctuations (in fact it is exponentially sensitive to the growth function at fixed mass); see Figure 12.22 and § 13.6. The LSST weak lensing selected lensing sample of mass selected clusters will be ideal for dark energy diagnostics.

Common two-point statistics, such as the cosmic shear power spectra (§ 14.4), do not contain all the statistical information of the WL field, and clusters are a manifestation of the non-Gaussian nature of the field. Recent studies (Fang & Haiman 2007; Takada & Bridle 2007) have shown that by combining the power spectrum with the redshift evolution of the cluster abundance, the constraints on dark energy parameters from shear power spectra can be tightened by roughly a factor of two.

However, even with photometric redshifts, one has little radial information (White et al. 2002; Hamana et al. 2004; Hennawi & Spergel 2005). All matter along the line-of-sight to the distant source galaxies contributes to the lensing signal. Consequently false detections of overdensities arise, due mostly to this projection effect: small mass objects along the same line of sight but physically separated in redshift would be attributed to a single object. Wang et al. (2009) suggest a simple alternative observable to cluster abundance, the fractional area of high significance hot spots in WL mass maps to determine background cosmological parameters. A similar idea is to use the projected WL peaks (Jain & Van Waerbeke 2000; Marian et al. 2008) regardless of whether they correspond to real galaxy clusters.

Here we focus on the fractional area of the high convergence regions, which has the advantage that it takes into account projection effects by construction. Analogous to the Press & Schechter (1974) formalism, it is determined by the high convergence tail of the probability distribution function (PDF). Previous works have shown that the one-point PDF is a simple yet powerful tool to probe non-Gaussian features (Reblinsky et al. 1999; Jain et al. 2000; Kruse & Schneider 2000; Valageas et al. 2005). Since the non-Gaussianity in the convergence field is induced by the growth of structure, it holds cosmological information mainly from the nonlinear regime and complements the well-established statistics in the linear regime.

Wang et al. (2009) used a Fisher matrix approach to forecast LSST cosmological parameter constraints with this method, dividing the galaxies into three bins with mean redshift $z_s = 0.6$, 1.1, and 1.9 so that each bin contains the same number of galaxies. They took a Gaussian smoothing scale of $\theta_G = 1$ arcmin, and considered seven different S/N thresholds, from $\nu = 2.0$ to 5.0 in increments of $\Delta\nu = 0.5$, in each redshift bin to utilize the information contained in the shape of the PDF. They assumed a 20,000 deg^2 survey with an rms shear noise of 0.047 per square arcminute, just slightly lower than the 0.05 cited in the introduction to this chapter, and a fiducial σ_8 of 0.9 (the assumed σ_8 has a strong effect on peak statistics). They also examined "pessimistic" and "optimistic" scenarios for systematic errors, the former being 1% priors on additive and multiplicative shear errors, and the latter being 0.01% and 0.05% priors respectively. (Note that neither of these accounts for photometric redshift errors.) They found, for example, a w_0 precision ranging from 0.55 for the pessimistic scenario to 0.16 for the optimistic scenario for LSST alone, decreasing to 0.12 and 0.043 respectively for LSST plus Planck priors.

Further theoretical work is needed to exploit this statistic. The one-point PDF has not been tested extensively in simulation for different cosmologies. For instance, Wang et al. (2009) adopt the expression given by Das & Ostriker (2006), which has been checked for only one flat ΛCDM cosmology with $\Omega_m = 0.3$. In order not to dominate the observational errors, the theoretical prediction for the PDF has to be accurate at the $\sim 1\%$ level, a level at which it has not been tested as a function of cosmological model. However, the one-point PDF is such a simple statistic, and its derivation adds almost no extra computational cost, once WL simulations are made. One expects to obtain accurately calibrated formulas for the PDF from currently ongoing or planned large WL simulations (§ 15.5).

14.4 Weak Lensing by Large-scale Structure

Lensing by large-scale structure (cosmic shear) is best characterized by two- and three-point correlation functions, or equivalently their Fourier transforms: power spectra. Much of the information contained in shear correlations measured by LSST will lie in the nonlinear regime of structure formation. Analytical models such as the halo model, N-body simulations, and hydrodynamical simulations (§ 15.5) are all required to obtain accurate predictions from arcminute to degree scales.

LSST will measure these correlation functions in source redshift shells, as well as cross-correlations between redshift shells. These correlations are sensitive to both the growth of structure and the expansion history of the Universe, making this a particularly powerful cosmological probe. The growth of structure can be separated from the expansion history in combination with expansion-history probes such as Type Ia Supernovae and baryon acoustic oscillations (§ 15.1), thus providing stringent tests of dark energy and modified gravity models.

14.4.1 Two-point Shear Correlations and Tomography

Bhuvnesh Jain, Anthony Tyson

To quantify the lensing signal, we measure the shear correlation functions from galaxy shape catalogs. The two-point correlation function of the shear, for source galaxies in the i^{th} and j^{th} redshift bin, is defined as

$$\xi_{\gamma_i\gamma_j}(\theta) = \langle \boldsymbol{\gamma_i}(\boldsymbol{\theta}_1) \cdot \boldsymbol{\gamma_j^*}(\boldsymbol{\theta}_2) \rangle, \tag{14.15}$$

with $\theta = |\boldsymbol{\theta}_1 - \boldsymbol{\theta}_2|$. Note that the two-point function of the convergence is identical to that of the shear. It is useful to separate ξ_γ into two separate correlation functions by using the $+/\times$ decomposition: the $+$ component is defined parallel or perpendicular to the line connecting the two points taken, while the $\times$ component is defined along 45°. This allows us to define the rotationally invariant two-point correlations of the shear field: $\xi_+(\theta) = \langle \gamma_{i+}(\boldsymbol{\theta}_1)\gamma_{j+}(\boldsymbol{\theta}_2) \rangle$, and $\xi_\times(\theta) = \langle \gamma_{i\times}(\boldsymbol{\theta}_1)\gamma_{j\times}(\boldsymbol{\theta}_2) \rangle$. The correlation function of Equation 14.15 is simply given by $\xi_{\gamma_i\gamma_j} = \xi_+ + \xi_-$.

There is information beyond tangential shear. The lensing signal is caused by a scalar potential in the lens and, therefore, should be curl-free. We can decompose each correlation function into one that measures the divergence (E-mode) and one that measures the curl (B mode). The measured two-point correlations can be expressed as contributions from E- and B-modes (given by linear superpositions of integrals over θ of ξ_+ and ξ_-). Since lensing is essentially derived from a scalar potential, it contributes (to a very good approximation) only to the E-mode. A more direct way to perform the E/B decomposition is through the mass aperture variance, $M_{\rm ap}^2(\theta)$, which is a weighted second moment of the tangential shear measured in apertures. This provides a very useful test of systematics in the measurements; we will not use it here, but refer the reader to Schneider et al. (2002). All two-point statistics such as $M_{\rm ap}^2(\theta)$ can be expressed in terms of the shear correlation functions defined above.

The shear power spectrum at angular wavenumber ℓ is the Fourier transform of $\xi_{\gamma_i\gamma_j}(\theta)$. It is identical to the power spectrum of the convergence and can be expressed as a projection of the mass density power spectrum, P_δ. For source galaxies in the i^{th} and j^{th} redshift bin, it is (Kaiser 1992; Hu 1999):

$$C_{\gamma_i\gamma_j}(\ell) = \int_0^\infty dz \, \frac{W_i(z)\, W_j(z)}{\chi(z)^2\, H(z)} \, P_\delta\!\left(\frac{\ell}{\chi(z)}, z\right), \tag{14.16}$$

where the indices i and j cover all the redshift bins. The geometric factors W_i and W_j are defined in Equation 14.4. The redshift binning is assumed to be provided by photometric redshifts (§ 3.8). The redshift binning is key to obtaining dark energy information from weak lensing. A wealth of cosmological information can be extracted by using shear-shear correlations, galaxy-shear cross-correlations (§ 14.2) and galaxy clustering in multiple redshift bins. As discussed in § 14.5, this must be done in the presence of several systematic errors, which have the potential to degrade errors on cosmological parameters. Note that if both source galaxy bins are taken at redshift z_s, then the integral is dominated by the mass fluctuations at a distance about half-way to the source galaxies. This is a useful guide in estimating the lens redshift best probed by a set of source galaxies.

Figure 14.3 shows the predicted power spectra from the ten-year LSST stack for galaxies split into three redshift bins: $z < 0.7$, $0.7 < z < 1.2$, $1.2 < z < 3$. The fiducial ΛCDM model is used for the predictions and the error bars indicate experimental uncertainty due to sample variance (which dominates at low ℓ) and shape noise (which dominates at high ℓ). The thin curves show the predictions for a $w = -0.9$ model. The figure shows that for much of the range in ℓ and z accessible

to LSST, such a model can be distinguished using a single bin alone (based on statistical errors); by combining the information in all bins, it can be distinguished at very high significance. Note that the actual measured power spectra include contributions from systematic errors, not included here but discussed in § 14.5. We also discuss below the covariance between spectra in different wavenumber bins due to nonlinear effects which degrade the errors at high ℓ. We have plotted just three spectra in Figure 14.3 for illustrative purposes. With LSST we expect to use many more bins, and also utilize cross-correlations between redshifts. About ten redshift bins exhaust the available weak lensing information in principle, but in practice up to twenty bins are likely to be used to carry out tests related to photometric redshifts and intrinsic alignments and to study questions such as the relation of luminous tracers to dark matter.

Equation 14.16 shows how the observable shear-shear power spectra are sensitive both to the geometric factors given by $W_i(z)$ and $W_j(z)$, and to the growth of structure contained in the mass density power spectrum, P_δ. Both are sensitive to dark energy and its possible evolution, which determine the relative amplitudes of the auto- and cross-spectra shown in Figure 14.3. P_δ also contains information about the primordial power spectrum and other parameters such as neutrino masses. In modified gravity theories, the shape and time evolution of the density power spectrum can differ from that of a dark energy model, even one that has the same expansion history. Lensing is a powerful means of testing for modifications of gravity as well (Knox et al. 2006; Amendola et al. 2008; Jain & Zhang 2008; Heavens et al. 2007; Huterer & Linder 2007). The complementarity with other probes of each application of lensing is critical, especially with the CMB and with measurements of the distance-redshift relation using Type Ia Supernovae and baryonic acoustic oscillations in the galaxy power spectrum.

The mass power spectrum is simply related to the linear growth factor $D(z)$ on large scales (low ℓ): $P_\delta \propto D^2(z)$. However, for source galaxies at redshifts of about 1, observable scales $\ell \gtrsim 200$ receive significant contributions from nonlinear gravitational clustering. So we must go beyond the linear regime using simulations or analytical fitting formulae to describe the nonlinear mass power spectrum (Jain & Seljak 1997; Jain et al. 2000; White 2004; Francis et al. 2007). To the extent that only gravity describes structures on scales larger than the sizes of galaxy clusters, this can be done with high accuracy. There is ongoing work to determine what this scale is precisely and how to model the effect of baryonic gas on smaller scales (Zentner et al. 2008), as discussed in more detail in § 14.5.4.

14.4.2 Higher-order Correlations

Masahiro Takada

Weak Lensing Covariances

It is important to understand the statistical precision of cosmic shear observables and error propagation in the determination of cosmological parameters. Since cosmic shear probes the projected mass distribution, the statistical properties of the cosmic shear field reflect those of the mass distribution. The statistical precision of the cosmic shear power spectrum is determined by the covariance, which contains three terms: shot noise contamination due to intrinsic ellipticities,

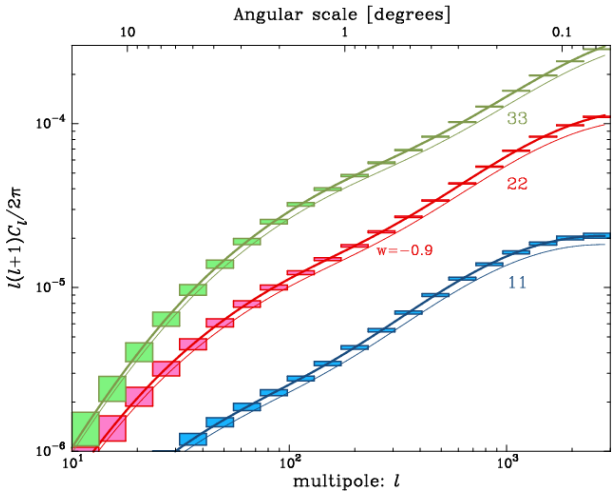

Figure 14.3: The lensing power spectra constructed from galaxies split into three broad redshift bins: $z < 0.7, 0.7 < z < 1.2$, and $1.2 < z < 3$. The solid curves are predictions for the fiducial ΛCDM model and include nonlinear evolution. The boxes show the expected measurement error due to the sample variance and intrinsic ellipticity errors (see text for details). The thin curves are the predictions for a dark energy model with $w = -0.9$. Clearly such a model can be distinguished at very high significance using information from all bins in ℓ and z. Note that many more redshift bins are expected from LSST than shown here, leading to over a hundred measured auto- and cross-power spectra.

and Gaussian and non-Gaussian sample variance caused by imperfect sampling of the fluctuations (Scoccimarro et al. 1999; Cooray & Hu 2001; Takada & Jain 2009). The non-Gaussian sample variance arises from the projection of the mass trispectrum weighted with the lensing efficiency kernel. In fact, most of the useful cosmological information contained in the lensing power spectrum lies on small angular scales, which are affected by nonlinear clustering. Therefore, the non-Gaussian errors can be significant in weak lensing measurements, and cannot be ignored in the precision measurements delivered by LSST.

The non-Gaussian errors cause two additional uncertainties in measuring the cosmic shear power spectrum. First, they degrade accuracies in measuring band powers of the spectrum at each multipole bin via the trispectrum contribution to the power spectrum covariance. Second, nonlinearities in the mass distribution cause correlations between the band powers at different multipoles, decreasing the effective number of independent degrees of freedom of multipoles measured from LSST.

Takada & Jain (2009) investigated the impact of the non-Gaussian errors on the cosmic shear power spectrum measurement using a dark matter halo approach. In the ΛCDM scenario, the cumulative signal-to-noise ratio for measuring the power spectrum over a range of angular scales, from degrees down to a few arcminutes scale, can be degraded by up to a factor of two compared to the Gaussian error case. Adding the tomographic redshift information slightly mitigates the degradation, but the non-Gaussian errors remain significant.

Given the LSST measurements, accuracies of estimating cosmological parameters can be obtained by propagating the statistical uncertainties of power spectrum measurements into parameter space. The marginalized errors on individual parameters would be degraded by less than 10-20% after the

proper analyses. The smaller degradation is primarily because: 1) individual parameters in a high-dimensional parameter space are degraded much less than the volume of the full Fisher ellipsoid in a multi-dimensional parameter space; 2) lensing involves projections along the line-of-sight, which reduce the non-Gaussian effect; and 3) some of the cosmological information comes from geometric factors which are not degraded at all. These are promising prospects; a large number of ray-tracing simulations will be needed to calibrate the impact of the non-Gaussian covariances on the parameter estimations, taking into account the effects of survey geometry and masking (§ 15.5).

Three-point Correlation Functions of Cosmic Shear

The non-Gaussian signatures measured via the higher-order moments themselves carry additional information that cannot be extracted with the power spectrum. In fact, the higher-order moments are complementary to the power spectrum because they depend differently on the lensing efficiency function, which in turn is sensitive to the geometry of the Universe. Takada & Jain (2004) showed that combining the three-point correlation of cosmic shear or the Fourier transform, bispectrum, with the power spectrum can improve the cosmological constraints by up to a factor of three.

However a more realistic forecast is needed that takes into account the non-Gaussian covariances of the bispectrum, which requires knowledge to the six-point correlation functions to calculate. The preliminary result is that bispectrum tomography is more degraded by non-Gaussian errors than is the power spectrum, but combining the two- and three-point correlation information can improve the dark energy constraints. This result indicates that most of the cosmological information inherent in cosmic shear can be extracted by using the two- and three-point correlation functions in CDM-dominated structure formation (we need not go to the four-point correlation!). This is because nonlinear clustering is physically driven by the quadratures of density and velocity perturbations in the continuity and Euler equations, which derive originally from Gaussian seed fluctuations. That is, the power spectrum gives us most of the Gaussian information in the original density field. The bispectrum encodes most of the non-Gaussian signatures that arise from nonlinear mode-coupling of the Gaussian field and the quadrature fields. The most important systematic in our understanding of the non-linear part of the mass spectrum is the effect of baryons (§ 14.5.4), which will have to modeled statistically.

The complementary sensitivities of the two- and three-point correlations to cosmological parameters offer a useful way of discriminating cosmological information from systematic errors in cosmic shear (such as shape measurement, photometric redshifts). The two- and three-point correlations are affected by these systematics in different ways. If we can model the systematic errors by physically motivated models with a small number of nuisance parameters, combining the two spectra allows determination of cosmological parameters and the nuisance parameters simultaneously, protecting the cosmological information against systematic errors – the self-calibration regime (Huterer et al. 2006). This method will be a powerful tool for controlling systematics and achieving the desired accuracy for constraining dark energy parameters with LSST.

14.5 Systematics and Observational Issues

LSST weak lensing using a sample of several billion galaxies provides wonderful statistical precision. Realizing that potential involves significant effort using multiple cross checks to detect and then control systematic errors. Here, we address observational systematics, including photometric redshift errors (§ 14.5.1), shear calibration and additive shear errors (§ 14.5.2), and intrinsic alignments of galaxies (§ 14.5.3). We also discuss our limited theoretical understanding of the effects of baryons on the small-scale lensing signal in § 14.5.4.

14.5.1 Photometric Redshift Systematics

David Wittman

Accurate inference of source galaxy redshifts is a fundamental requirement for weak lensing. The photometric redshift performance of the LSST survey is discussed in § 3.8. Here we discuss how photometric redshift errors relate to weak lensing science, and how systematics can be controlled to the required level.

Unlike some other science areas, in weak lensing and in BAO, the accuracy and precision of the photometric redshifts, z_p, matter less than how well we *know* the distribution function of photometric redshift errors in any photometric redshift bin. Because the weak lensing kernel is broad in redshift, wide photometric redshift bins may be used. The science analysis proceeds by integrating over the distribution and is biased only to the extent that the assumed distribution is incorrect. In the simplified case of a Gaussian distribution, Huterer et al. (2006) found that the mean and scatter of the distribution should be known to about 0.003 in each redshift bin. Ma & Bernstein (2008) extended this to arbitrary distributions, which can be represented as a sum of Gaussians, but this more sophisticated analysis did not qualitatively change the result. Huterer et al. (2006) also investigated the effect of z_p systematics on combined two-point and three-point statistics, and found that requirements are much reduced: with only a 20-30% dark energy constraint degradation, z_p errors could be self-calibrated from the data (§ 14.4.2). However, this assumed a very simple z_p error model, and so may be overly optimistic. It may not be necessary to reach a precision of 0.003 per bin for precision cosmology: combining WL and BAO data can significantly reduce the required photometric redshift precision (§ 15.1).

It is traditional to "measure" the z_p bias and scatter by obtaining spectroscopic redshifts of a subset of galaxies. If this were true, the spectroscopic sample requirement is simply to amass a large enough sample to beat down the noise in each bin to less than 0.003. In this context, Ma & Bernstein (2008) estimate that $10^5 - 10^6$ spectroscopic redshifts would be sufficient for LSST. However, estimates of bias and scatter from the $z_p - z_s$ relation contain systematics because the spectroscopic sample is never completely representative of the photometric sample, especially for deep photometric surveys where spectroscopy cannot go as faint as the photometry. Even for less deep surveys ($r \sim 24$), the spectroscopic incompleteness rate is a function of type, magnitude, color, and redshift (e.g., Cannon et al. 2006).

We are currently modeling photometric redshifts with the LSST filter set and depth to better understand the range of possible systematic errors. We have already found one way to dramatically reduce systematic errors, namely using a full probability distribution, $p(z)$, rather than a single

point estimate for each galaxy (Wittman 2009). Mandelbaum et al. (2008b) also found this in the context of galaxy-galaxy lensing. We plan to store a full $p(z)$, or a compressed version of it, for each galaxy.

Systematic errors in the z_p distribution will be a function of type, color, magnitude and redshift. We are planning a "super-photometric redshift" field observed in a large number of filters by the time of LSST commissioning to calibrate these quantities; see § 3.8.4. We are also developing a new method of calibrating redshift distributions using angular cross-correlations with a spectroscopic sample (Newman 2008); see § 3.8.5 for more details. One potential difficulty relates to lensing: magnification induces angular cross-correlations between foreground structures and background galaxy populations (Bernstein & Huterer 2009). However, the deep fields can be used to characterize the fainter population available for magnification into the gold sample, and thus correct for this effect.

14.5.2 Shear Systematics

Shear Calibration

David Wittman, Anthony Tyson

The primary systematic of concern in weak lensing is the smearing of galaxy shapes due to the telescope point-spread function (PSF). LSST delivered image quality will be good, with a nominal $0.7''$ FWHM cutoff for weak lensing observations, but it still will be a challenge to accurately infer the true shapes of galaxies, which are often smaller than this.

There are many contributions to the PSF: atmospheric turbulence or "seeing," optics and perturbations on the optics, non-flatness of the focal plane and the CCDs, charge diffusion in the detector, etc. Simulations that include these effects are discussed in detail in § 3.3. Here we discuss these issues as they relate to weak lensing specifically and describe how systematics will be controlled to the required level.

If the PSF were perfectly round (isotropic), it would change galaxy shapes by making them appear more round, thus diluting the lensing signal. Recovering the true amplitude of the shear is a problem referred to as *shear calibration*, or reducing multiplicative errors. Real PSFs are themselves anisotropic, and thus may imprint *additive* shear systematics onto the galaxies, as we discuss in the next subsection. In any case, the observed galaxy shape is the true galaxy shape convolved with the PSF. Thus, for barely resolved galaxies, this effect is very large and must be removed to high precision. Huterer et al. (2006) found that for LSST to maintain precise dark energy constraints, shear must be calibrated to 0.1%. And as with photometric redshifts, they found that combining the two- and three-point functions substantially reduced this requirement.

The current state of the art is 1% calibration accuracy, based on blind analysis of simulated data (Heymans et al. 2006b; Massey et al. 2007a). The lensing community is now working with the statistics community, bringing in new ideas through blind analysis challenges (Bridle et al. 2008). Meanwhile, the LSST Weak Lensing Science Collaboration is developing LSST-specific ways to reduce this problem. Among them are:

- MultiFit as described in detail in § 2.5.2, whereby properties of each galaxy are determined not by a co-addition of all the images covering a given field, but by a simultaneous fit to each image. This uses the PSF information of each exposure in an optimal way, and thus should allow maximal control of PSF-related systematics.
- Jain et al. (2006) suggested a method of canceling out many PSF-related errors: when computing correlation functions, *cross*-correlate shapes from two separate sets of images of a given field. The PSFs are independent, so the correlation functions should be free of PSF-related systematics, again barring a very global systematic. This idea can be combined with the previous idea by cross-correlating shapes produced by MultiFit from two separate sets of 100 exposures each, for example.
- High-fidelity image simulations as described in § 3.3 are underway to test the LSST pipeline's ability to model the PSF. Subtle effects such as color dependence of the PSF from differential chromatic refraction will be included.
- Jarvis & Jain (2004) demonstrated the effectiveness of principal component analysis (PCA) for accurately modeling PSF variations in data sets where many images were taken with the same instrument. LSST is the ultimate in this regard, with several *million* images to be taken by a single camera. The PCA can also be augmented with a physically motivated optical model (Jarvis et al. 2008), which takes advantage of the extensive modeling done for LSST.

Simulations including everything from all relevant cosmological effects to PSF distortions due to the atmosphere and telescope optics, will be invaluable for testing this machinery. Typically one checks for systematics by measuring the B-mode, which should be very near zero in the absence of systematics. However, multiplicative errors can change the E-mode more than they change the B-mode, by up to an order of magnitude (Guzik & Bernstein 2005). The LSST image simulator (§ 3.3) will allow these tests to be carried out. The LSST deep fields (§ 2.1) will also be valuable for assessing the accuracy of shear measurements using the faintest galaxies, by comparing shear measurements using only the main imaging data and those using the deep data.

Additive Shear Errors

David Wittman

Even if shear calibration were perfect, spurious shear can be added by an anisotropic PSF. In this section we highlight several tests that demonstrate that this effect can be controlled to high precision. There are three main sources of PSF anisotropy: focal plane, optics, and atmosphere.

In long-exposure astronomical images, PSF anisotropy induced by atmospheric turbulence is negligible because the turbulence flows across the aperture and averages out after several seconds. LSST's exposure time of 15 seconds is just short enough that atmospheric anisotropy must be considered. Wittman (2005) examined a set of 10 and 30 second exposures from the Subaru Telescope, which is a good match to LSST, with roughly the same aperture and a wide field camera (Suprime-Cam). These exposures contained a high density (8 arcmin^{-2}) of well-measured stars; a randomly selected subset representing typical survey densities ($\sim$ 1 arcmin^{-2}) were used to build a PSF model and the remaining $\sim$7 stars arcmin^{-2} used to assess residuals. On the 0.3-3 arcminute scales examined, the residual "shear" correlations were 1–2 orders of magnitude below the

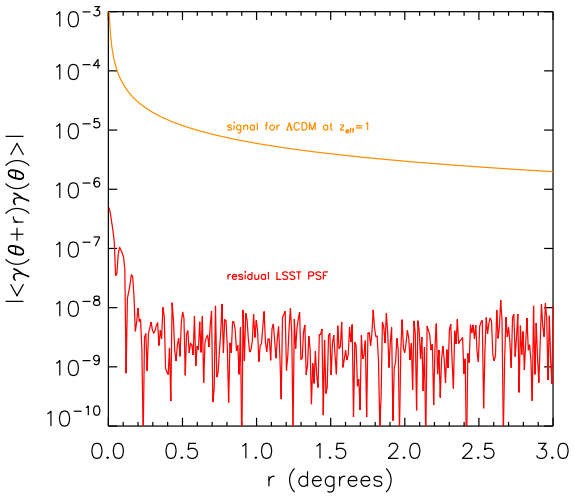

Figure 14.4: Absolute value of shear residuals as a function of angular separation, for a simulated exposure. As described in the text and in Jee et al. (2007), the simulated image includes atmosphere, perturbed LSST optics, and focal plane non-flatness. The simulation included zero true lensing signal, thus assessing additive errors only. About one high-S/N star arcmin^{-2} (close to the density that the LSST data will have) was used to model the spatial variation of the PSF, while many additional point sources were used to assess the residuals (a luxury we will not have with the real data!). LSST *statistical* errors on the shear will be roughly 1% of the lensing signal for the scales shown here. Note that because the absolute value is shown, residuals are actually consistent with zero beyond 0.25°.

cosmological signal in a single exposure, and were further averaged down by multiple exposures. After five exposures, the residuals were less than the projected LSST statistical error on scales 3 arcmin and larger. On larger scales, the effects of the atmosphere falls off quite rapidly, and other systematics are more worthy of attention as described below. On smaller scales, it seems likely that this systematic will be well controlled with hundreds of LSST exposures, but large data sets or simulations will be required to prove this assertion.

Jee et al. (2007) extended this type of analysis to 3° scales using simulated star fields (§ 3.3) imaged through a simulated atmosphere, a model of the LSST optics with realistic perturbations, and simulated focal plane departures from flatness, including piston errors and potato chip curvature of the sensors. Figure 14.4 shows the residual correlations in a single image full of high-S/N stars. The residuals are three orders of magnitude less than the lensing signal out to 0.25° scales, beyond which they are consistent with zero (Figure 14.4 shows the absolute value of the residuals; in fact, the sign fluctuates at large scales). For comparison, LSST statistical errors are typically about two orders of magnitude smaller than the signal over the range of scales shown. Note that this discussion applies to additive errors only, as the simulations lacked input shear. More sophisticated simulations are now being assembled to assess the ability to recover a given input shear.

The Power of Many Exposures

The large number of exposures in the LSST survey provides built-in advantages for reducing shear errors. Hundreds of dithered exposures per filter at various pupil rotations and image rotations will

help isolate and reduce systematics. In addition to the MultiFit, PCA, and cross-image correlation methods described above, the LSST data set will enable many windows into systematics which are not available today. For example, one could divide the data set into seeing bins and examine the trends of cosmic shear with seeing. Furthermore, the LSST scheduler will be able to *control* some important aspects such as instrument rotation, so that each field will be seen by many different rotations and dither positions. This will allow us to *examine* the systematics in many different subsets and use this information to further control systematics.

14.5.3 Intrinsic Alignments of Galaxies

Rachel Mandelbaum

Weak lensing analyses begin with the assumption that galaxy shapes are uncorrelated in the absence of gravitational shears. Intrinsic alignments of galaxy shapes violate this assumption, and are typically due to correlations with local tidal fields and/or the larger scale cosmic web. ΛCDM N-body simulations and analytic models show that such alignments of dark matter halos are expected on large scales (Croft & Metzler 2000; Heavens et al. 2000; Catelan et al. 2001; Crittenden et al. 2001; Jing 2002; Hopkins et al. 2005), but the question of whether observed galaxy shapes, i.e., the shapes of the baryonic components, also show such alignments cannot be answered with N-body simulations. While many observational studies have found intrinsic alignments within structures such as galaxy groups and clusters (e.g., Binggeli 1982; Fuller et al. 1999; West & Blakeslee 2000; Pereira & Kuhn 2005; Agustsson & Brainerd 2006; Faltenbacher et al. 2007), of greater concern are alignments that persist on the large scales used for cosmological lensing studies.

Alhough this section focuses on intrinsic alignments as a contaminant to lensing surveys, these alignments are also an interesting problem in galaxy formation. In brief, observations of intrinsic alignments can help us learn 1) how the shape of a galaxy is affected by tidal fields as it is formed; 2) how that shape evolves with time given the (also-evolving) tidal field of large-scale structure; and finally, 3) how galaxy interactions and mergers erase information about the original projected shapes of the galaxies. Because these questions depend on the galaxy formation history, we expect the intrinsic alignment signal to depend on morphology, luminosity, and possibly environment (and thus redshift).

To determine the effects of intrinsic alignments on the measured lensing signals, we express the shape of a galaxy as the sum of three shear terms,

$$\gamma = \gamma_{\rm rand} + \gamma_I + \gamma_G. \tag{14.17}$$

The first term is simply the random shape and orientation of the galaxy on the sky, the second is the tidal shear that causes intrinsic alignment with local or large-scale structures, and the third is the gravitational lens shear from foreground mass. In the absence of γ_I, shear-shear autocorrelations (cosmic shear) simply measure $\langle\gamma_G\gamma_G\rangle$. However, if $\gamma_I \neq 0$, the shear-shear autocorrelation signal acquires two additional terms, $\langle\gamma_I\gamma_I\rangle$ and $\langle\gamma_G\gamma_I\rangle$.

The $\langle\gamma_I\gamma_I\rangle$ term (e.g., Croft & Metzler 2000), often known as the II alignment, is due to the fact that galaxies that experience the same local tidal field become aligned with that field and, therefore, with each other. Consequently, this term is important only for two galaxies at the

same redshift. The $\langle \gamma_G \gamma_I \rangle$ term (Hirata & Seljak 2004), often known as the GI alignment, arises when a tidal field at some redshift causes intrinsic alignment of a galaxy at that redshift, and also gravitationally shears a more distant galaxy, anticorrelating their shapes. Similarly, one can define intrinsic alignment terms for any other lensing statistic determined using galaxy shape measurements (e.g., three-point functions have GGI, GII, and III intrinsic alignment terms).

Because intrinsic alignments are difficult to predict theoretically, observational measurements have attempted to determine at what level these alignments will contaminate the lensing signal for surveys such as LSST. Observations of II alignments at low redshift (Mandelbaum et al. 2006b; Okumura et al. 2008) suggest that while II alignments may be present at a low level particularly for luminous red galaxies, these alignments should affect the cosmic shear signal for an LSST-like survey at the several percent level (at most) if not removed. The GI term, which has been robustly detected for red galaxies to tens of Mpc, may be more important than the II term, possibly contaminating the estimated σ_8 inferred from the cosmic shear signal for an $r < 24$ survey at the -2% level, or most pessimistically -10% (Mandelbaum et al. 2006b; Hirata et al. 2007). Our current understanding will likely be supplemented in the coming years with constraints for fainter and bluer galaxies, and at higher redshift. It is clear, however, that an LSST-like survey must estimate and remove this GI alignment term.

The use of photometric redshifts to avoid correlating galaxies at the same redshift can eliminate II alignments (King & Schneider 2002; Heymans & Heavens 2003; King & Schneider 2003; Takada & White 2004). Unfortunately, this scheme will actually exacerbate the GI alignments, since the GI alignment depends on the correlation with a gravitational shear that increases as the pair separation in redshift space increases. However, Joachimi & Schneider (2008, 2009) have explored a method that works perfectly in the presence of spectroscopic redshifts to remove both the II and GI terms, based on their known dependence on the redshifts of the galaxy pairs. This geometric scheme results in the loss of some statistical power that depends on the number of redshift bins, as quantified in Joachimi & Schneider (2008), but typically expands the areas of confidence regions in parameter space by several tens of percent for a large number of bins. Joachimi & Schneider (2009) show that the need to remove intrinsic alignments in this way places stringent requirements on the photometric redshift quality.

Other schemes, such as that proposed by King (2005), project out the II and GI terms using some dependence on galaxy type, redshift, transverse separation on the sky, and luminosity. In that case, observations that already have constrained these dependencies serve as model inputs, so that one can avoid losing as much information as when using the Joachimi & Schneider (2008) method. Bridle & King (2007) find that intrinsic alignments can double the number of tomographic bins required to recover 80% of the available information from the lensing analysis, while requiring three times smaller photometric redshift errors than in the case of no intrinsic alignment contamination. However, 10%-level priors on the intrinsic alignment power spectrum, which should be achievable given data that will be available at the start of LSST, are very helpful in minimizing information loss due to intrinsic alignments.

Other useful diagnostics that may help minimize the contamination of the LSST cosmic shear measurement by intrinsic alignments include the intrinsic alignments three-point functions (Semboloni et al. 2008), the galaxy-galaxy lensing signal, and the B-mode signal (Hirata & Seljak 2004; Heymans et al. 2006c; Bridle & King 2007). Since most of the weak lens source galaxies are faint

and blue, and no significant alignment for that population has yet been found, it is possible that the intrinsic alignment corrections will be small.

14.5.4 Theory Systematics: The Effect of Baryons

Andrew Zentner

Utilizing shear correlations to constrain dark energy puts demands on theorists to make accurate predictions for these quantities. In particular, the matter power spectrum must be computed on scales $k \sim$ a few Mpc^{-1} to better than a percent to render biases in dark energy parameters negligible (Huterer & Takada 2005). This goal may be achievable with dissipationless N-body simulations of cosmological structure growth in the near future. However, current N-body calculations amount to treating all matter as dark matter and neglecting the non-gravitational interactions of the baryonic component of the Universe during structure growth and the gravitational response of the dark matter to the redistribution of baryons (§ 15.5). The process of galaxy formation is not well understood in its detail, and this introduces a potentially important theoretical uncertainty in predictions of lensing observables. However, it is likely that this challenge can be addressed adequately and weak lensing observables from LSST used to constrain the physics of both dark energy and galaxy formation.

Following earlier analytic studies (White 2004; Zhan & Knox 2004), recent simulations have addressed the influences of baryonic processes on lensing observables. Alhough results differ in their details, all studies indicate that baryonic effects can modify lensing statistics relative to dissipationless N-body predictions by amounts that are large compared to the statistical limits of LSST (Jing et al. 2006; Rudd et al. 2007). If unaccounted for, these offsets translate into biases in dark energy parameters comparable to or larger than their statistical uncertainties (Zentner et al. 2008). One could apply a nulling procedure to mitigate the contamination of small-scale processes, but the cost is a factor of ~ 3 increase in dark energy equation-of-state constraints and a corresponding factor of ~ 10 decrease in the Dark Energy Task Force (Albrecht et al. 2006) figure of merit (Zentner et al. 2008).

It should be feasible to model such effects in the near future and salvage much of the information contained in the high-multipole range of the power spectrum. The power spectra of the Rudd et al. (2007) simulations differ from N-body results in a regular fashion. These authors showed that the bulk of the difference is due to markedly different mass distributions within dark matter halos in baryonic simulations compared to the same halos in N-body simulations. To the degree that this is valid, standard N-body-based techniques can be corrected for baryonic effects, eliminating biases on scales $\ell < 5000$, by modifying the internal structures of halos. Scales of $\ell < 2000$ are important for cosmic shear.

It is necessary to re-assess cosmological constraints in models that contain the additional parameter freedom of a baryonic correction. Zentner et al. (2008) studied the influence of the additional parameter freedom on dark energy constraints from shear power spectra under various assumptions on the relationship between halo concentration and mass. With reliable tomographic binning, the additional freedom is not strongly degenerate with dark energy and the degradation in the constraints on w_0 and w_a is less than 20% in one specific (and reasonable) model for the concentration. Alternatively, theoretical or observational prior knowledge of the concentrations of halos

near $M \sim 10^{14}h^{-1}\mathrm{M}_{\odot}$ of better than 30% significantly reduce the influence of the degradation due to baryonic effects on halo structure (Zentner et al. 2008). Contemporary constraints from galaxy-galaxy lensing are already approaching this level (Mandelbaum et al. 2008a). This is also constrained by requiring consistency with galaxy-galaxy lensing. Finally, strong+weak lensing precision studies of several thousand clusters, taken together with optical and X-ray data, will constrain baryon-mass models.

A comprehensive simulation program is underway to assess baryonic effects, understand them, and account for them (§ 15.5). This program will result in a robust treatment of lensing observables measured with LSST and will be a boon for galaxy modelers as well. Internal calibration of halo structure in an analysis of shear spectra will translate into valuable information about galaxy formation. The program has two aspects. One is to simulate several self-consistent models of galaxy formation in cosmologically large volumes. Such simulations are limited due to computational expense. The second aspect is to treat baryonic processes with effective models that are not self-consistent, but aim to capture the large-scale dynamical influences of baryonic condensation and galaxy formation in a manner that is computationally inexpensive. This second set of simulations allows for some exploration of the parameter space of cosmology and baryonic physics.

14.5.5 Systematics Summary

We have examined both multiplicative and additive shear systematics. Multiplicative systematics arise from the convolution of a galaxy image with a finite PSF. These systematics are a function of galaxy size relative to the PSF and the limiting surface brightness of the image. Additive shear systematics arise from anisotropic PSFs and also depend on galaxy size. We have described above how the telescope design, survey strategy, and algorithmic advances incorporated into the LSST image analysis will enable us to control and mitigate shear systematics.

Our methods need to be thoroughly tested through simulations, such as the ones we discussed in this chapter, § 3.3, and § 15.5. One of the most challenging areas for systematics will be at large scales. Many of the tests we have cited apply mostly to small scales of a focal plane or less. The current record for largest scale cosmic shear detection is 4°, which is just larger than an LSST focal plane. The cosmic shear signal is small at very large scales and experience is limited. However, large scales do have some advantages, such as the large number of PSF stars. More work must be done to assure the control of systematics on these scales including simulations of different dither patterns.

Beyond shear systematics, the three primary sources of systematics we addressed relate to photometric redshifts, intrinsic alignments, and theoretical uncertainties. While advances in methodology and modeling will help mitigate these, empirical information will provide the surest check. Thus for both photometric redshift errors and intrinsic alignments, spectroscopic data at high redshifts will enable us to calibrate and marginalize over the systematic error contributions. For the uncertainty in theoretical predictions at small scales, a powerful consistency check (within the halo model framework) will be provided by high precision measurements of the shear profiles of clusters of different masses. Thus the LSST data set will itself provide the most reliable test of the theoretical model.

References

Agustsson, I., & Brainerd, T. G., 2006, *ApJL*, 644, L25
Albrecht, A. et al., 2006, Astrophysics eprints, ArXiv:astro-ph/0609591
Amendola, L., Kunz, M., & Sapone, D., 2008, *Journal of Cosmology and Astro-Particle Physics*, 4, 13
Bardeen, J. M., Bond, J. R., Kaiser, N., & Szalay, A. S., 1986, *ApJ*, 304, 15
Bartelmann, M., King, L. J., & Schneider, P., 2001, *A&A*, 378, 361
Bartelmann, M., & Schneider, P., 2001, *Phys. Rep.*, 340, 291
Bernstein, G., & Huterer, D., 2009, ArXiv e-prints, 0902.2782
Binggeli, B., 1982, *A&A*, 107, 338
Bond, J. R., Cole, S., Efstathiou, G., & Kaiser, N., 1991, *ApJ*, 379, 440
Bradač, M. et al., 2006, *ApJ*, 652, 937
Bradač, M., Schneider, P., Lombardi, M., & Erben, T., 2005, *A&A*, 437, 39
Bridle, S., & King, L., 2007, *New Journal of Physics*, 9, 444
Bridle, S. et al., 2008, ArXiv e-prints, 0802.1214
Broadhurst, T. J., Taylor, A. N., & Peacock, J. A., 1995, *ApJ*, 438, 49
Cannon, R. et al., 2006, *MNRAS*, 372, 425
Catelan, P., Kamionkowski, M., & Blandford, R. D., 2001, *MNRAS*, 320, L7
Clowe, D., Bradač, M., Gonzalez, A. H., Markevitch, M., Randall, S. W., Jones, C., & Zaritsky, D., 2006a, *ApJL*, 648, L109
Clowe, D., Luppino, G. A., Kaiser, N., & Gioia, I. M., 2000, *ApJ*, 539, 540
Clowe, D., & Schneider, P., 2001, *A&A*, 379, 384
Clowe, D. et al., 2006b, *A&A*, 451, 395
Cooray, A., & Hu, W., 2001, *ApJ*, 554, 56
Crittenden, R. G., Natarajan, P., Pen, U.-L., & Theuns, T., 2001, *ApJ*, 559, 552
Croft, R. A. C., & Metzler, C. A., 2000, *ApJ*, 545, 561
Das, S., & Ostriker, J. P., 2006, *ApJ*, 645, 1
Dietrich, J. P., Erben, T., Lamer, G., Schneider, P., Schwope, A., Hartlap, J., & Maturi, M., 2007, *A&A*, 470, 821
Dubinski, J., & Carlberg, R. G., 1991, *ApJ*, 378, 496
Fahlman, G., Kaiser, N., Squires, G., & Woods, D., 1994, *ApJ*, 437, 56
Faltenbacher, A., Li, C., Mao, S., van den Bosch, F. C., Yang, X., Jing, Y. P., Pasquali, A., & Mo, H. J., 2007, *ApJL*, 662, L71
Fang, W., & Haiman, Z., 2007, *Phys. Rev. D*, 75, 043010
Francis, M. J., Lewis, G. F., & Linder, E. V., 2007, *MNRAS*, 380, 1079
Fuller, T. M., West, M. J., & Bridges, T. J., 1999, *ApJ*, 519, 22
Gavazzi, R., & Soucail, G., 2007, *A&A*, 462, 459
Guzik, J., & Bernstein, G., 2005, *Phys. Rev. D*, 72, 043503
Haiman, Z., Mohr, J. J., & Holder, G. P., 2001, *ApJ*, 553, 545
Hamana, T., Takada, M., & Yoshida, N., 2004, *MNRAS*, 350, 893
Heavens, A., Refregier, A., & Heymans, C., 2000, *MNRAS*, 319, 649
Heavens, A. F., Kitching, T. D., & Verde, L., 2007, *MNRAS*, 380, 1029
Hennawi, J. F., & Spergel, D. N., 2005, *ApJ*, 624, 59
Heymans, C. et al., 2006a, *MNRAS*, 371, L60
Heymans, C., Brown, M., Heavens, A., Meisenheimer, K., Taylor, A., & Wolf, C., 2004, *MNRAS*, 347, 895
Heymans, C., & Heavens, A., 2003, *MNRAS*, 339, 711
Heymans, C. et al., 2006b, *MNRAS*, 368, 1323
Heymans, C., White, M., Heavens, A., Vale, C., & van Waerbeke, L., 2006c, *MNRAS*, 371, 750
Hirata, C. M., Mandelbaum, R., Ishak, M., Seljak, U., Nichol, R., Pimbblet, K. A., Ross, N. P., & Wake, D., 2007, *MNRAS*, 381, 1197
Hirata, C. M., & Seljak, U., 2004, *Phys. Rev. D*, 70, 063526
Hoekstra, H., Hsieh, B. C., Yee, H. K. C., Lin, H., & Gladders, M. D., 2005, *ApJ*, 635, 73
Hoekstra, H., Yee, H. K. C., & Gladders, M. D., 2004, *ApJ*, 606, 67
Hopkins, P. F., Bahcall, N. A., & Bode, P., 2005, *ApJ*, 618, 1
Hu, W., 1999, *ApJL*, 522, L21
Huterer, D., & Linder, E. V., 2007, *Phys. Rev. D*, 75, 023519
Huterer, D., & Takada, M., 2005, *Astroparticle Physics*, 23, 369

Huterer, D., Takada, M., Bernstein, G., & Jain, B., 2006, *MNRAS*, 366, 101
Jain, B., Jarvis, M., & Bernstein, G., 2006, *Journal of Cosmology and Astro-Particle Physics*, 2, 1
Jain, B., & Seljak, U., 1997, *ApJ*, 484, 560
Jain, B., Seljak, U., & White, S., 2000, *ApJ*, 530, 547
Jain, B., & Taylor, A., 2003, *Phys. Rev. Lett.*, 91, 141302
Jain, B., & Van Waerbeke, L., 2000, *ApJL*, 530, L1
Jain, B., & Zhang, P., 2008, *Phys. Rev. D*, 78, 063503
Jarvis, M., & Jain, B., 2004, Astrophysics e-prints, arXiv:astro-ph/0412234
—, 2008, *Journal of Cosmology and Astro-Particle Physics*, 1, 3
Jarvis, M., Schechter, P., & Jain, B., 2008, Astrophysics e-prints, 0810.0027
Jee, M. J. et al., 2007, Bulletin of the American Astronomical Society, Vol. 38, Ellipticity Correlation of the LSST PSF and Optimal Interpolation Scheme. p. 983
Jenkins, A., Frenk, C. S., White, S. D. M., Colberg, J. M., Cole, S., Evrard, A. E., Couchman, H. M. P., & Yoshida, N., 2001, *MNRAS*, 321, 372
Jing, Y. P., 2002, *MNRAS*, 335, L89
Jing, Y. P., Zhang, P., Lin, W. P., Gao, L., & Springel, V., 2006, *ApJL*, 640, L119
Joachimi, B., & Schneider, P., 2008, *A&A*, 488, 829
—, 2009, ArXiv e-prints, 0905.0393
Johnston, D. E. et al., 2007, ArXiv e-prints, 0709.1159
Kaiser, N., 1992, *ApJ*, 388, 272
Kaiser, N., & Squires, G., 1993, *ApJ*, 404, 441
Kaiser, N., Squires, G., & Broadhurst, T., 1995, *ApJ*, 449, 460
Khiabanian, H., & Dell'Antonio, I. P., 2008, *ApJ*, 684, 794
King, L., & Schneider, P., 2002, *A&A*, 396, 411
King, L. J., 2005, *A&A*, 441, 47
King, L. J., & Schneider, P., 2003, *A&A*, 398, 23
Knox, L., Song, Y.-S., & Tyson, J. A., 2006, *Phys. Rev. D*, 74, 023512
Kruse, G., & Schneider, P., 2000, *MNRAS*, 318, 321
Ma, Z., & Bernstein, G., 2008, *ApJ*, 682, 39
Mackey, J., White, M., & Kamionkowski, M., 2002, *MNRAS*, 332, 788
Mandelbaum, R., Hirata, C. M., Broderick, T., Seljak, U., & Brinkmann, J., 2006a, *MNRAS*, 370, 1008
Mandelbaum, R., Hirata, C. M., Ishak, M., Seljak, U., & Brinkmann, J., 2006b, *MNRAS*, 367, 611
Mandelbaum, R., Seljak, U., & Hirata, C. M., 2008a, *Journal of Cosmology and Astro-Particle Physics*, 8, 6
Mandelbaum, R. et al., 2008b, *MNRAS*, 386, 781
Mandelbaum, R., Seljak, U., Kauffmann, G., Hirata, C. M., & Brinkmann, J., 2006c, *MNRAS*, 368, 715
Marian, L., Smith, R. E., & Bernstein, G. M., 2008, ArXiv e-prints, 0811.1991
Markevitch, M., Gonzalez, A. H., Clowe, D., Vikhlinin, A., Forman, W., Jones, C., Murray, S., & Tucker, W., 2004, *ApJ*, 606, 819
Massey, R. et al., 2007a, *MNRAS*, 376, 13
—, 2007b, *Nature*, 445, 286
Milgrom, M., 1983, *ApJ*, 270, 365
Miyazaki, S., Hamana, T., Ellis, R. S., Kashikawa, N., Massey, R. J., Taylor, J., & Refregier, A., 2007, *ApJ*, 669, 714
Newman, J. A., 2008, *ApJ*, 684, 88
Okumura, T., Jing, Y. P., & Li, C., 2008, ArXiv e-prints, 0809.3790
Parker, L. C., Hoekstra, H., Hudson, M. J., van Waerbeke, L., & Mellier, Y., 2007, *ApJ*, 669, 21
Pereira, M. J., & Kuhn, J. R., 2005, *ApJL*, 627, L21
Press, W. H., & Schechter, P., 1974, *ApJ*, 187, 425
Reblinsky, K., Kruse, G., Jain, B., & Schneider, P., 1999, *A&A*, 351, 815
Rudd, D. H., Zentner, A. R., & Kravtsov, A. V., 2007, *ApJ*, 672, 19
Sackett, P. D., 1999, *Astronomical Society of the Pacific Conference Series*, 182, 393
Sanders, R. H., 1986, *MNRAS*, 223, 539
Schneider, P., van Waerbeke, L., Jain, B., & Kruse, G., 1998, *MNRAS*, 296, 873
Schneider, P., van Waerbeke, L., & Mellier, Y., 2002, *A&A*, 389, 729
Scoccimarro, R., Zaldarriaga, M., & Hui, L., 1999, *ApJ*, 527, 1
Seitz, C., & Schneider, P., 1997, *A&A*, 318, 687

Seitz, S., & Schneider, P., 1996, *A&A*, 305, 383
Seitz, S., Schneider, P., & Bartelmann, M., 1998, *A&A*, 337, 325
Semboloni, E., Heymans, C., van Waerbeke, L., & Schneider, P., 2008, *MNRAS*, 388, 991
Sheldon, E. S. et al., 2001, *ApJ*, 554, 881
—, 2007, ArXiv e-prints, 0709.1153
Sheth, R. K., & Tormen, G., 1999, *MNRAS*, 308, 119
Springel, V. et al., 2005, *Nature*, 435, 629
Takada, M., & Bridle, S., 2007, *New Journal of Physics*, 9, 446
Takada, M., & Jain, B., 2004, *MNRAS*, 348, 897
—, 2009, astro-ph/0810.4170, astro-ph/0810.4170
Takada, M., & White, M., 2004, *ApJL*, 601, L1
Tyson, J. A., & Fischer, P., 1995, *ApJL*, 446, L55
Tyson, J. A., Wenk, R. A., & Valdes, F., 1990, *ApJL*, 349, L1
Valageas, P., Munshi, D., & Barber, A. J., 2005, *MNRAS*, 356, 386
Wang, S., Haiman, Z., & May, M., 2009, *ApJ*, 691, 547
West, M. J., & Blakeslee, J. P., 2000, *ApJL*, 543, L27
White, M., 2004, *Astroparticle Physics*, 22, 211
White, M., van Waerbeke, L., & Mackey, J., 2002, *ApJ*, 575, 640
Wittman, D., 2005, *ApJL*, 632, L5
—, 2009, ArXiv e-prints, 0905.0892
Wittman, D., Dell'Antonio, I. P., Hughes, J. P., Margoniner, V. E., Tyson, J. A., Cohen, J. G., & Norman, D., 2006, *ApJ*, 643, 128
Wittman, D., Margoniner, V. E., Tyson, J. A., Cohen, J. G., Becker, A. C., & Dell'Antonio, I. P., 2003, *ApJ*, 597, 218
Zentner, A. R., Rudd, D. H., & Hu, W., 2008, *Phys. Rev. D*, 77, 043507
Zhan, H., & Knox, L., 2004, *ApJL*, 616, L75